Received 28 November 2020; revised 18 January 2021; accepted 28 January 2021. Date of publication 4 February 2021; date of current version 2 March 2021.

Digital Object Identifier 10.1109/OJAP.2021.3057135

A Metamaterial Position Sensor Based on Magnetoinductive Waves

J. YAN, C. J. STEVENS (Member, IEEE), AND E. SHAMONINA (Member, IEEE)

Department of Engineering Science, University of Oxford, Oxford OX1 3PJ, U.K.

CORRESPONDING AUTHOR: J. YAN (e-mail: jiaruo.yan@eng.ox.ac.uk)

The work of J. Yan was supported by Metaboards Ltd., through Russell Studentship Project "Directivity of Metamaterial-Based Antennas." The work of C. J. Stevens and E. Shamonina was supported by the Engineering and Physical Sciences Research Council, U.K., under Grant EP/N010493/1 (SYMETA).

ABSTRACT In this article we report our first investigations of a new contactless localizing sensor based on the propagation of slow waves in metamaterials. Using the properties of magnetoinductive waves in a one dimensional metamaterial we are able to unambiguously locate a nearby object. This works because when an object impinges on the near field of the metamaterial's meta-atoms, it introduces a local defect resulting in the reflections of magnetoinductive waves. Key performance metrics are investigated and the ultimate horizontal range of the sensor is demonstrated to be directly linked to the metamaterials quality. An algorithm is devised based on the standing waves modes. The effect of terminating the structure with a matching impedance is discussed. Unambiguous localization of a single object is possible using a low-complexity algorithm, when the object interacts strongly with the metamaterial structure.

INDEX TERMS Electromagnetic coupling, electromagnetic metamaterials, localization, sensor.

I. INTRODUCTION

NON-MECHANICAL human-machine interfaces has been a key driver to the development of many technologies over the last 20 years. So called 'touch sensitive' displays have, in particular become almost ubiquitous since their adoption for smartphone design [1], [2], [3], [4]. The majority of these rely on variations in the mutual capacitance between adjacent electrodes which are arranged in a dense grid. The electrode grid is fabricated using transparent conductors and placed above the display. Readout of the electrode grid is done by polling them in pairs requiring many measurements and making the readout electronics relatively complex [5]. Whilst touch screens are very advanced they have several drawbacks, one of which is their short range and insensitivity - no capacitive touch screen works well through gloves for instance.

Reducing the complexity [6] of the readout for touch screens is a potentially rewarding research target, with the ultimate goal being readout of position with a single measurement. To this end we have begun investigating a number of novel propagation media to enable one and two dimensional localization via confined waves [7]. Using a suitable algorithm we aim to determine the point of interaction between an object and the surface exchanging physical complexity for computational effort.

As a starting point we chose to use a well known metasurface formed from simple meta-atoms. Meta-atoms in this context are electromagnetic objects designed to have a particular resonant or non-resonant set of electric and magnetic susceptibilities whilst being much smaller in size than the wavelength of the signals with which they interact - for example a simple split ring resonator [8]. Meta-atoms are generally combined to form metamaterials [9] of one sort or another. A one or two dimensional arrangement of meta-atoms is often referred to as a meta-surface [10]. Metasurfaces in which the meta-atoms exhibit some degree of mutual coupling (either by electric or magnetic fields for instance) will generally support some kind of wavelike signal propagation. Examples of this include slow waves like those carried by magnetoinductive waveguides [11].

Because meta-atoms and metasurfaces interact with the force-fields they are exposed in, they are sensitive to their environment and many sensor applications are being developed. These include displacement sensors [12], [13], [14], sensors for dielectric characterization [15], [16], [17], [18], strain gauges [19], [20], and touched systems using a mixture of waveguides and

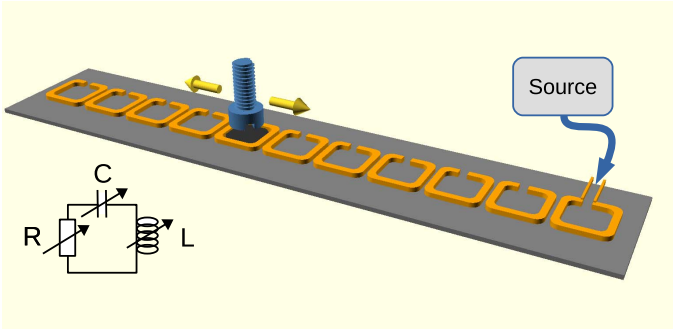

FIGURE 1. Magnetoinductive waveguide formed from magnetically coupled split ring resonators supporting slow waves along its length. Waves can be launched from the source connection, and a metal object (bolt) in close proximity creates a strong defect at the 7^{th} cell from the source. Inset is the LCR resonator circuit used to describe the impact of induced defects.

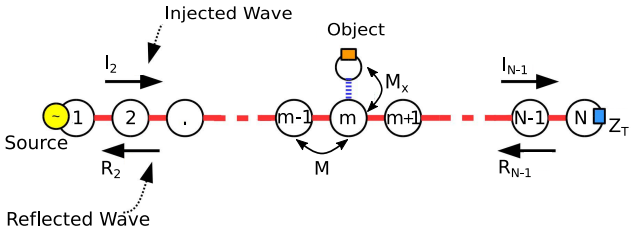

FIGURE 2. Simplified sketch representing the cells of the MIW, the source injecting waves, the object to be localized interacting with its nearest neighbouring cell *m* and the termination impedance Z_T of the last cell *N*.

meta-atoms [21]. Sensors and detection systems based on MI waves have been studied in [22], [23], [24].

As a starting point for future work we have investigated a simple one dimensional line of meta-atoms that are coupled together by mutual inductance forming a magnetoinductive waveguide (MIW) [11]. In this work we are exploring the use of such MIW as 'touch' sensors detecting the presence and location of a nearby metallic object in air. Such systems may also be demonstrated in two dimensional surfaces in the future.

II. THEORETICAL BACKGROUND

A. MAGNETOINDUCTIVE WAVEGUIDES AS SENSORS

Fig. 1 shows the basic construction of our device which uses a magnetoinductive waveguide (MIW) with an object (for example a metal bolt) interacting with the meta-atoms to create a defect. Here a source injects signals at the first meta-atom which propagate down the line, scattering from the defect along the way and forming a standing wave pattern of circulating currents. Our earlier work explored the properties of slow waves [11], [25] in these structures and the potential for these structures to provide a data channel [26], or a medium for wireless power delivery [27]. We have found that MIW structures are readily modelled using circuit theory based on the Kirchoff equations. Absorbing terminations added to the end of the MIW suppress the reflections from the structure [28]. A broadband transducer capable of low-loss coupling between the MIW and a real load has been introduced [29]. In addition, waveguides, in which electric and magnetic coupling both play a role, have been developed [30], [31], [32].

MIW carry signals across a passband whose width is mostly a function of the strength of the meta-atoms mutual coupling. Signals injected (using a small loop antenna for instance) that are within this passband will travel through the MIW and reflect from an un-terminated end forming standing waves. The outcome from the source point of view is a modulated input impedance or scattering parameter (S_{11}). Using a first neighbour approximation the bandwidth is defined by

$$\Delta f = f_0 \left[\frac{1}{\sqrt{1-|\kappa|}} - \frac{1}{\sqrt{1+|\kappa|}} \right] \tag{1}$$

where $\kappa = 2M/L$ in which L is the self-inductance of the rings and M is their mutual inductance. MIW can be made with i) simple split rings, and ii) rings loaded with tuning elements. In the case i) the resonators are sensitive to changes in their electromagnetic environment, whilst for case ii) the electric interactions are suppressed and they are mostly susceptible only to magnetic or conductive changes.

B. METAMATERIAL LOCALIZATION - MIW REFLECTANCE AND INPUT IMPEDANCE

Within the bandwidth defined by (1), waves propagate to the end of the line according to the dispersion which is quite non-linear

$$\gamma\, d = \operatorname{acosh}\left(\frac{-Z}{2X}\right) \tag{2}$$

where $\gamma\, d$ is the complex propagation coefficient per period [11]. Z is the cell impedance ($Z = R + j\omega L - j/\omega C$ for an LCR resonator as shown by the inset in Fig. 1, R, L, C being the resistance, the self-inductance, and the self-capacitance of the resonator), and X is the mutual impedance between two adjacent resonators ($X = j\omega M$ for a magnetic system like that shown in Fig. 1). In the following we inject signals into a line of N cells, at the start of the line (cell 1) and measure the input impedance. The object is adjacent to cell m. A simple scheme for this is shown in the cellular diagram of Fig. 2 where the object is represented by an extra element that couples to the m^{th} cell of the line.

Waves reflect from the end of the MIW at cell N, because there is no element after there to support them, with reflection coefficient ρ_T equal to the ratio of incident I_{N-1} and reflected R_{N-1} current amplitudes. We define $\rho_T = \rho_{N-1}$ in terms of the amplitudes of waves at cell $N-1$ where they can be unambiguously defined. Without a load, and if losses are low, this is near unity. If something modifies the properties of the m^{th} cell of an MIW by a big enough factor (see Fig. 2), then magnetoinductive waves are reflected by that cell as we previously derived [27]. In this earlier work we were calculating the wireless power transfer to a resistive load driven by a receiver brought into proximity with the

MIW. Now, our intention is to obtain the spectrum of the input impedance Z_{in} presented by the MIW when a target object perturbs the loop impedance $Z = R + j\omega L - j/\omega C$ of the m^{th} cell. By analysing this impedance we want to determine the location of the perturbation and hence of the target object.

Localizing the object for intermediate positions, i.e., between two adjacent cells, would require a more comprehensive model that takes into account the impact of the conductive object on the mutual inductance M, which was discussed in [33], [34], [35]. This is neglected in this article, and satisfying results for discrete localization (when the object is above centres of the cells) have been obtained.

Our method in brief relies on using the relationship between the reflectance of a termination cell and the impedance of that cell. Using the properties of MIW, we can refer any terminating impedance back to any other point on the line as described in detail in [27]. First one requires the reflectance of the line termination ρ_{T}

$$\rho_{\text{T}}(Z_{\text{T}}) = \frac{X^2 - (Z + Xe^{\gamma\, d})(Z + Z_{\text{T}})}{(Z + Xe^{-\gamma\, d})(Z + Z_{\text{T}}) - X^2} \tag{3}$$

where Z_{T} is an extra impedance added to the last cell of the line as a termination - generally zero in our case of a line of identical cells. Based on (3), we can rearrange the equation to get an expression of effective termination impedance that would give an MIW reflectance of ρ_{N-1}

$$Z_{\text{T}}^{N} = \frac{X^2(1 + \rho_{N-1})}{Z(1 + \rho_{N-1}) + X(\rho_{N-1}e^{-\gamma d} + e^{\gamma d})} - Z \tag{4}$$

We need to determine the reflectance ratio ρ_{m-1} measured just before the defect cell m. This then requires a value for the extra impedance Z_{T}^{m} in the modulated defect cell m. The extra impedance is due to the nearby perturbing object, along with the effective termination impedance due to the cells between the defect and the end of the line. The reflectance ρ_m, at cell m, is given by

$$\rho_m = \rho_{\text{T}}\, e^{-2(N-m-1)\gamma d} \tag{5}$$

The equivalent terminal impedance Z_{T}^{m+1} at cell $m+1$, is evaluated using (4), replacing ρ_{N-1} by ρ_m. The defect cell m has then an effective terminal impedance

$$Z_{\text{T}}^{m} = Z_{\text{defect}} + Z_{\text{eff}} \tag{6}$$

where Z_{defect} is the change in impedance of the defect due to the object, and Z_{eff}, the impedance presented by cell $m+1$ to cell m is [27]

$$Z_{\text{eff}} = -X^2/(Z_{\text{T}}^{m+1} + Z) \tag{7}$$

Therefore, the reflectance evaluated at cell $m-1$, ρ_{m-1}, can be obtained by substituting $Z_{\text{T}}^{(m)}$ into Z_{T} in (3), as we may now treat the defect cell like a termination [27].

To evaluate the overall input impedance Z_{in} seen by the source, the additional impedance at cell 1 due to the rest of the line are calculated in a similar process (by referring ρ_{m-1} to the injection point and calculating the input impedance Z_{in}) using (3) - (5). The input reflectance is given by

$$\rho = \frac{Z_{\text{in}} - Z_{\text{ref}}}{Z_{\text{in}} + Z_{\text{ref}}} \tag{8}$$

where Z_{ref} is the reference impedance.

In order to evaluate the defect reflectance from which to model the impact of an object, we conduct a simple experiment with a single loaded split ring resonator. Our devices are made as Printed Circuit Boards (PCBs) carrying resonators which are squares 10 mm on a side with width 1 mm. Each of these resonators is tuned by adding a 100 pF surface mount capacitor, which among other impacts, reduced the resonators overall sensitivity to its dielectric environment by containing the majority of the electric field energy. Magnetic fields are not so contained and permeate each cell's local environment making them sensitive to any objects able to perturb those fields. In our models the resonators are simple resonant circuits composed of an inductor (L), capacitor (C) and resistor (R). The resistor models all the losses present in the resonators including ohmic, dielectric and radiation contributions [36] as drawn in Fig. 1.

The highly conducting metal object (steel M6 bolt head, hexagonal, 10 mm diameter) is placed axially above the resonator and moved towards it from 12 mm separation to near contact. The resonant frequency f_0 of the system is measured along with its Q factor, shown in Fig. 3(a).

When the loaded resonator is approached by the metal object, its resonant frequency f_0 rises whilst its Q factor falls - denoting both a decrease in the $L-C$ product and a rise in the loss (R). This makes the model for the modulation of the split ring by the object quite simple. With the metal object (bolt), we decrease the inductance and raise the losses in the form of eddy currents. The extracted R and L are plotted in Fig. 3(b). It should be noted that although we conducted the measurements using a bolt at varying heights above a single resonator, similar detuning effects can be obtained using bolts of varying sizes at a fixed height above the resonator. Decreasing the size of the bolt head leads to weaker interactions between the object and the resonator below, i.e., creating smaller changes in the inductance and less resistive losses in the resonator. As an example, a steel bolt head of 7 mm diameter, placed at 0.4 mm above the resonator and with the centres aligned, results in $L_{\text{defect}} \approx 17.1$ nH and $R_{\text{defect}} \approx 0.29\Omega$ in the measurements, which is very close to what we measured with an M6 bolt at 1 mm above the resonator.

The reflectance from the defect ρ_{m-1}, calculated at cell $m-1$, for varying object height z is shown in Fig. 3(c). The termination is included as $Z_{\text{T}} = X\exp(-\gamma\, d)$ in series with the self-impedance of the last cell to remove reflections from the end [9]. Here $m = 8$, but the defect can be anywhere on the line except for the two ends. As z increases, the interactions between the object and the defect cell become weaker, leading to lower reflectance from the defect. When z is above around 6 mm, L_{defect} and R_{defect} approach the

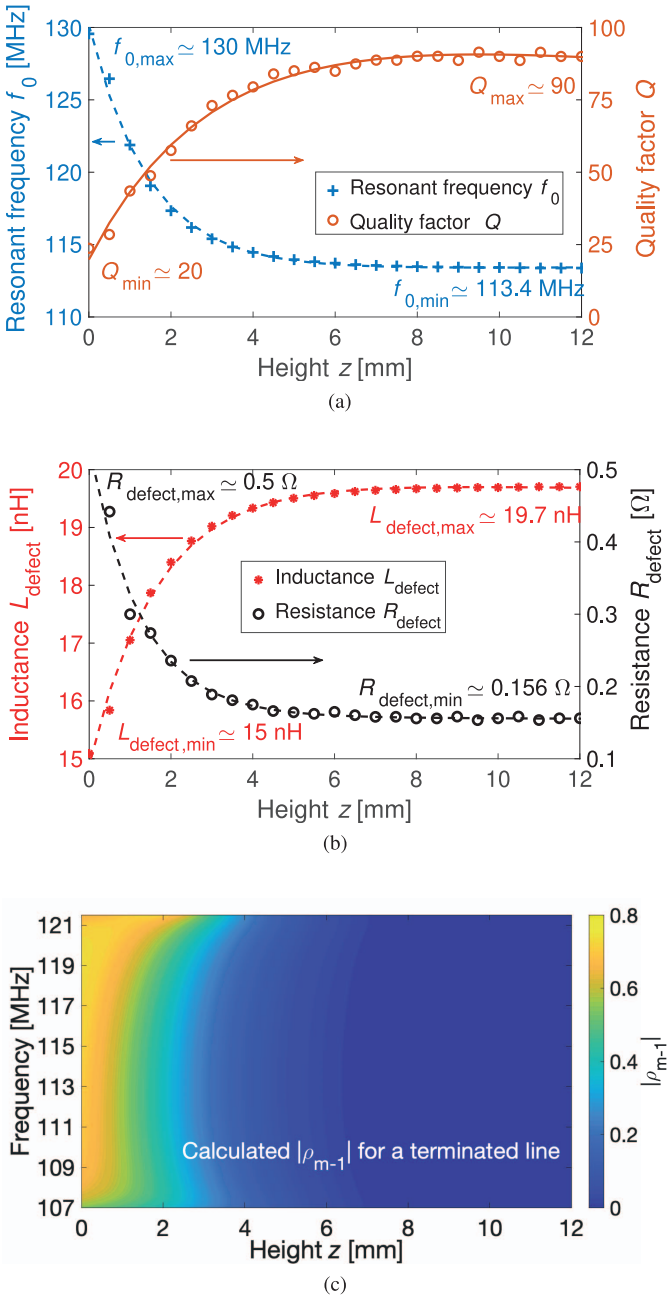

FIGURE 3. Impact of a highly conducting object, the head of a metal bolt, as a function of its height above one meta-atom which is a loaded PCB split ring. Measured resonance characteristics, f_0 (blue plus signs), Q (orange circles), of the meta-atom in (a) are convertible to equivalent circuit parameters, L_{defect} (red asterisks) and R_{defect} (black circles), in (b). The solid curves in (a) and (b) are the fitted curves to the measured data points. As z increases from 0 to 12 mm, the resonance f_0 changes from 130 to 113.4 MHz, quality factor Q from 20 to 90, the inductance of the element L_{defect} from 15 to 19.7 nH and resistance R_{defect} from 0.5 to 0.16 Ω. The end values for these parameters are the unperturbed values for the element. (c) is the calculated variation of $|\rho_{m-1}|$, the net reflectance from the defect evaluated at cell $m-1$, with the elevation z of the metal object. The end of the 16-element array is terminated with a matching impedance [9], and defect can be anywhere on the line except for the two ends.

unperturbed values as shown in Fig. 3(b), therefore the array approaches an infinite line. The net reflectance from the defect is slightly larger for higher frequencies within the passband. This is due to the increased resonant frequency of the perturbed defect cell.

Waves travelling in an array of N elements from one end to the other will mostly reflect back and form standing waves which have integral numbers of half periods. The propagation coefficients of the N standing wave modes are [11]

$$k_n = \frac{2\pi}{\lambda_n} = \frac{\pi}{(n+1)d}, n = 1, 2, 3 \cdots N \tag{9}$$

where λ_n is the wavelength of the n-th order mode, d is the lattice period. The N standing wave frequencies also correspond to the resonances exhibited by an array of N coupled resonators, the reflectance from which also shows local minima at these frequencies.

The sensor relies on the development of these standing waves in the line, between the reflective defect and the source. If the modulation of the input impedance produced by these standing waves is significant then we may determine the existence and location of the defect. The benefit of this is that only one source is required for input impedance probing. Here, one may use the properties of MIW to determine the maximum length of sensor that can be useful, beyond which we won't be able to discriminate the standing wave patterns for different defect positions. For an infinitely long sensor no reflections are expected from the end, only those arising from a defect. These result in a series of peaks in the input impedance spectrum. In general as the location of the defect moves away from the source then the frequency spacing between standing wave peaks in the spectrum shrinks. Eventually these peaks become unresolvable and we are unable to discern the location of the induced defect produced by the object.

The resolvability of the peaks will be limited by their width which is in turn linked to the meta-atom quality factor as LCR circuits. Using (5) we can determine a relationship between the meta-atom quality factor and the useful length of a device in terms of the modulation depth for adjacent peaks in the impedance spectrum. Because the object reflectance varies slowly with frequency as shown in Fig. 3(c), the reflectance at a standing wave peak and its neighbouring trough is nearly the same. The only change between peak and trough is the π difference in phase for the signals reflected arriving at the source. This consideration allows us to write the variation in current in the injection cell at this frequency as:

$$\Delta I = (I_0 + \rho_+ I_0) - (I_0 - \rho_- I_0) \approx 2\rho_{m-1} I_0 e^{-2(m-1)\alpha d} \tag{10}$$

where the input current I_0 launches waves into the structure and the reflected waves contribute $\rho_{+/-} I_0$ to the overall amplitude. $\rho_{+/-}$ are the reflectance at peak and trough frequencies respectively. For a relatively low loss MIW the attenuation can be approximated to $\alpha d = (\kappa Q)^{-1}$. If one sets a threshold on the modulation depth that permits effective localization - say $\Delta I/I_0 = 0.1$ - then one may derive:

$$N_{max} = 1 - \frac{\kappa Q}{2} \ln\left(\frac{\Delta I/I_0}{2\rho_{m-1}}\right) \tag{11}$$

where N_{max} is the ultimate length after which no object can produce peak-trough modulation depth greater than $\Delta I/I_0$,

and we have assumed a perfectly matched source. Clearly there is a strong linear dependence between N_{max} and the Q factor for the meta-atoms. It's also clear that objects which interact less strongly with the meta-atoms, producing a lower defect reflectance ρ_{m-1} will result in a shorter ultimate horizontal length for a given modulation depth.

III. RESULTS

A. ANALYTICAL CALCULATIONS

Based on the derivations earlier, we calculate the reflectance $|\rho|$ as a function of frequency at the input when the object is moved along a line at a height of 0.4 mm above the cells, as shown in Fig. 4(a). We only consider discrete object locations above cell centres as explained in Section II-B. We use the corresponding values $L_{\text{defect}} = 15.9\,\text{nH}$, $R_{\text{defect}} = 0.43\,\Omega$ from Fig. 3(b) for the calculations. To evaluate the reflectance for a notionally matched source driving the device we used $Z_{\text{ref}} = 4\,\Omega$ so that the calculated reflectance is of similar magnitudes and comparable to measured values.

For the first meta-atom of the line (position 1), it's clear that the detuning effect of the object is changing the self-resonance, resulting in a single minimum of $|\rho|$ at around 129 MHz. Moving the object to position 2 results in a single strong minimum at 113 MHz - this being now close to the unperturbed resonant frequency of the source cell. there is also a weak minimum at around 129 MHz. As the object moves further along the device, away from the source, the number of these strong standing wave troughs increases whilst their resolvability decreases with reduced frequency separation as expected. If one were to apply a $\Delta I/I_0 = 0.1$ modulation depth limit and $\rho_m = 0.5$ then (11) predicts that this device should be capable of locating an object up to 16 cells distance.

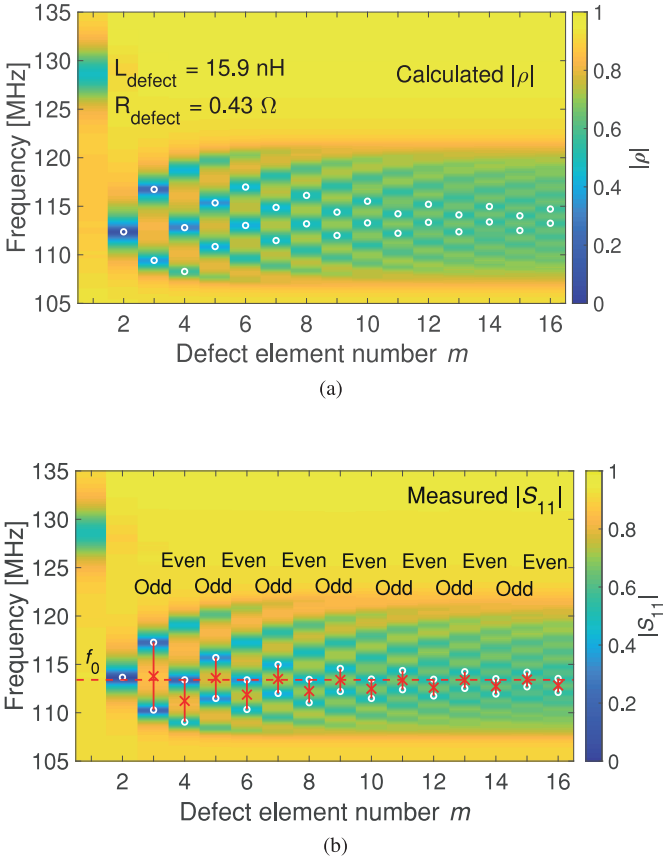

FIGURE 4. Calculated reflectance and measured $|S_{11}|$ spectrum for metal object locations above cell centres. (a) Calculated reflectance $|\rho|$ from (3)–(5) with parameters: $\kappa = -0.13$, $L_{\text{defect}} = 15.9\,\text{nH}$, $f_0 = 113.4\,\text{MHz}$. $Z_{\text{ref}} = 4\,\Omega$ is used. (b) Measured $|S_{11}|$ from the MIW. The metal object is moved at 0.4 mm above the structure. The loop antenna is placed below the centre of cell 1. The white circles in both (a) and (b) marks the local minima in the reflectance or S_{11} that are used in our Odd-Even algorithm introduced in Section III-C, and the 'x' markers show their mean oscillating above and below the resonant frequency. The resonant frequency is shown by the dashed horizontal line.

B. EXPERIMENT

We have developed an experiment to test our ability to locate a metal object near to a MIW as an example to match the calculations in the previous section. The waveguide used in the experiments is an array of 16 strongly coupled identical square resonators.

Our structure is made as a Printed Circuit Board (PCBs) carrying resonators which are squares 10 mm on a side with track width 1 mm. The FR4 substrate is 1.6 mm thick. A 100 pF surface mount capacitor is added to the 1 mm gap on each of these resonators, and every cell exhibits a resonant frequency of 113.4 MHz. The lattice period, which is the centre-to-centre separation between the adjacent cells, is 10.5 mm. The measured nearest-neighbour coupling coefficient is $\kappa = 2M/L \approx -0.13$. The metal object we used in the experiment is a steel M6 bolt head, of hexagonal shape and 10 mm diameter. We used plastic holders to attach the metal object to the scanning arm of the 2D scanner, and also to fix the source loop antenna in place below the array.

A small loop antenna 5 mm in diameter located 1.6 mm below the first meta-atom is used to inject signals. The S_{11} input scattering parameter here is recorded by connecting the loop antenna to a VNA and the metal bolt is moved along the device at a height of around 0.4 mm above the structure, in 0.5 mm horizontal steps. The 2D scanner is connected to a PC which controls the scanning process. The height of the metal bolt ensures that the inductance of the element dropped from 19.7 nH, the unperturbed value, to around 15.9 nF when the bolt centre is aligned axially with a cell's centre. The recorded S_{11} over frequency is shown in Fig. 4(b), where the x-axis shows the bolt location measured in periods of the metamaterial, with each integer value corresponding to the cell number where the bolt perfectly centres above that meta-atom.

The measured S_{11} is shown in Fig. 4(b) where it may be readily compared to the calculated spectrum of Fig. 4(a). Both are quite comparable with the large detuning of the first element when the bolt is located at position 1 and a gradually increasing number of standing wave minima as it moves down the line away from the source. At first glance, counting the number of minima seems to be a viable method for locating the bolt based on the reflection spectrum. Whilst

this is straightforward if one has a high quality measurement of the S_{11} spectrum, should one seek to reduce equipment complexity and use only a narrow range of the spectrum, the optimal path is less obvious. Further complications arise when the object is higher, permitting more waves to travel to the end of the line, adding extra standing wave modes.

C. METHOD FOR LOCATION EXTRACTION

The frequencies of the standing wave modes may be predicted from the dispersion relationships. Therefore, we devised a method to localize the metal bolt based on the unique frequency patterns of the array. In the following we denote the defect cell number as m. First, for each centred defect location, we identified the frequencies that correspond to local minima in $|\rho|$. Since the reflectance pattern becomes unresolvable out near the cut-off frequencies due to increasing MIW loss, we concentrated on the frequencies near the middle of the passband at $f_0 = 113.4$ MHz. For all even m, there is a minimum in the S_{11} very close to f_0, whereas for odd $m > 1$, there is a weak maximum near f_0 and two local minimums at frequencies almost symmetrical about f_0. We used the two minima in $|\rho|$ closest to the f_0, and we denoted these corresponding frequencies as f_a and f_b.

1) STANDING WAVE-BASED ALGORITHM

Having determined f_a and f_b as a subset of the standing wave modes of the composite structure plus defect, our first attempt for localization is to calculate the frequency difference $\delta f = |f_a - f_b|$ and to compare it with the value calculated based on the theoretical dispersion relationships of (2). The exceptions are, when the object is above the cell 1 or 2, no dips or only one dip would be found within the passband. The result for testing this algorithm on the measured data is that, 11 out of the total 16 centre locations can be retrieved accurately, while the remaining 5 positions are identified with ± 1 lattice period error. This most likely arises from the fact that the theoretical dispersion assumes only first order coupling between meta-atoms whilst in the real structure this is not the case and results in slightly distorted dispersion and thus shifted standing wave modes [11].

2) ODD-EVEN ALGORITHM

To improve on this result, an additional condition is imposed to categorize m as an even or odd number. This is done based on the average of f_a and f_b - if $|(f_a + f_b)/2 - f_0| > \delta$, m is even, otherwise the object should be above an odd-numbered element, where $\delta = 0.53$ MHz is a chosen threshold that gives zero error in localization up to $m = 16$. For larger arrays, optimization of δ could be needed, if second order coupling is significant. After applying this additional condition, all 16 locations are found accurately, using both the calculated reflectance and the measured S_{11} data. The process of the algorithm is summarized in Fig. 5. The limitation is that only discrete centre locations have been considered, and intermediate localization will be studied in the future.

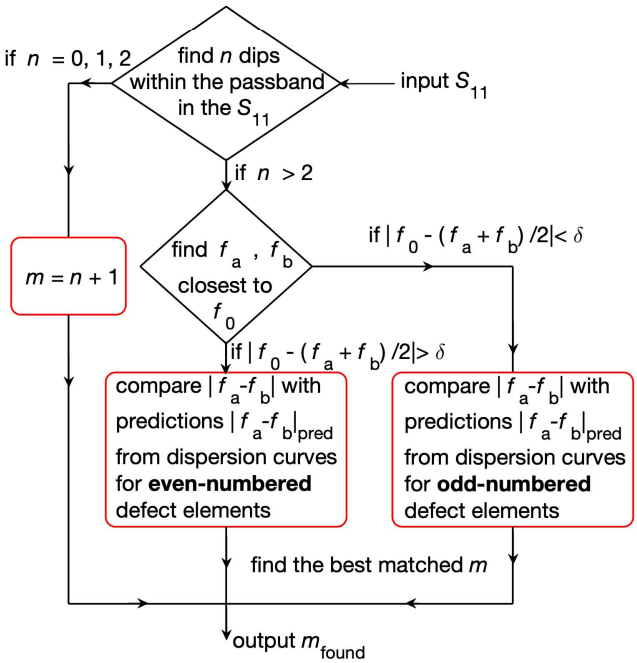

FIGURE 5. Flow chart illustrating the Odd-Even algorithm for localization. The input to the algorithm is the reflectance or S_{11} spectrum.

With a large change in the impedance of the defect element when the object is very close, there are clear dips in the input reflectance spectrum, shown by the blue spots in Fig. 4. However, when the interaction between a defect and the object is weaker, some of the injected waves amplitude will be reflected back to the source from both the defect and the far end of the array. Superposition of these reflection signals at the source results in more complicated standing wave patterns. Taking $L_{\text{defect}} = 18.5$ nH, the calculated reflectance pattern is shown in Fig. 6(a). The corresponding resistance of the defect element is $R_{\text{defect}} = 0.22\,\Omega$ [from Fig. 3(b)], which was achieved when the metal bolt used in the experiment is around 2 mm above the defect centre. The minimum reflectance at $m = 2$ is around 0.4, higher than the strong minimum of 0.04 when $z = 0.4$ mm, showing a smaller change in the value of the input reflectance with frequency. For all the defect locations there is now a strong background signature of waves reflecting from the far end of the array with more than 9 minima visible. When the standing modes of the source - defect section of the line coincide in frequency with the background component, there is enhancement of the peaks and troughs. Terminating the array by adding an impedance $Z_T = X \exp(-\gamma d)$ [9] eliminates this background component and the resultant reflectance pattern is shown in Fig. 6(b).

We tested the Odd-Even algorithm on the calculated $|\rho|$ patterns generated using a range of defect inductance values to explore the impact of the partial reflectance of the defect. L_{defect} varies between 15 nH and the undisturbed value of 19.7 nH. This range of L_{defect} values can be obtained by positioning the metal object at varying heights above a single

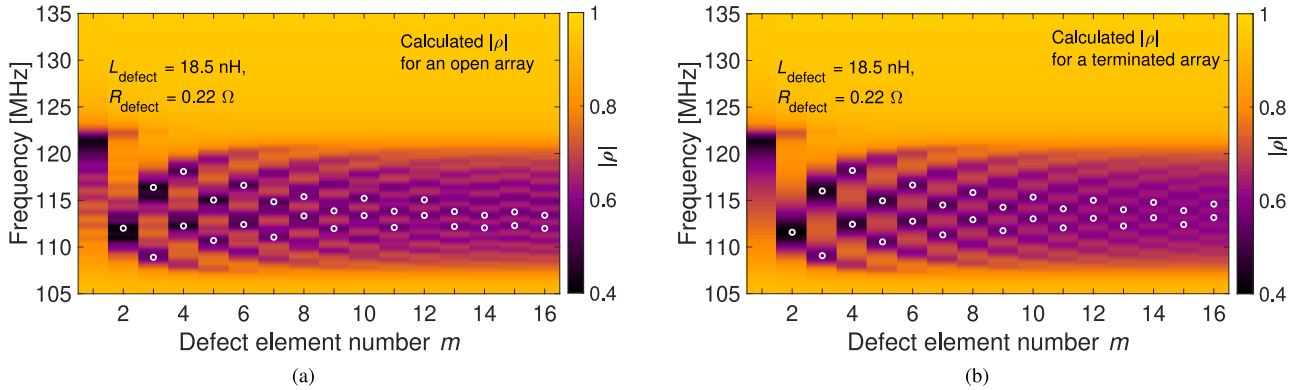

FIGURE 6. Calculated reflectance $|\rho|$ spectrum for defect locations from cell 1 to 16, when the inductance of defect element is 18.5 nH (L_0 of an undisturbed cell is 19.7 nH). (a) The 16-element array is an open array. Reflections from both the defect element and the end of the array lead to multiple dips in the reflectance spectrum, which degrades the performance of our Odd-Even algorithm. (b) The end of the line is now terminated with a matching impedance, eliminating the reflections from the end of the array [9]. The white circles mark the dips that are used in our Odd-Even localization algorithm.

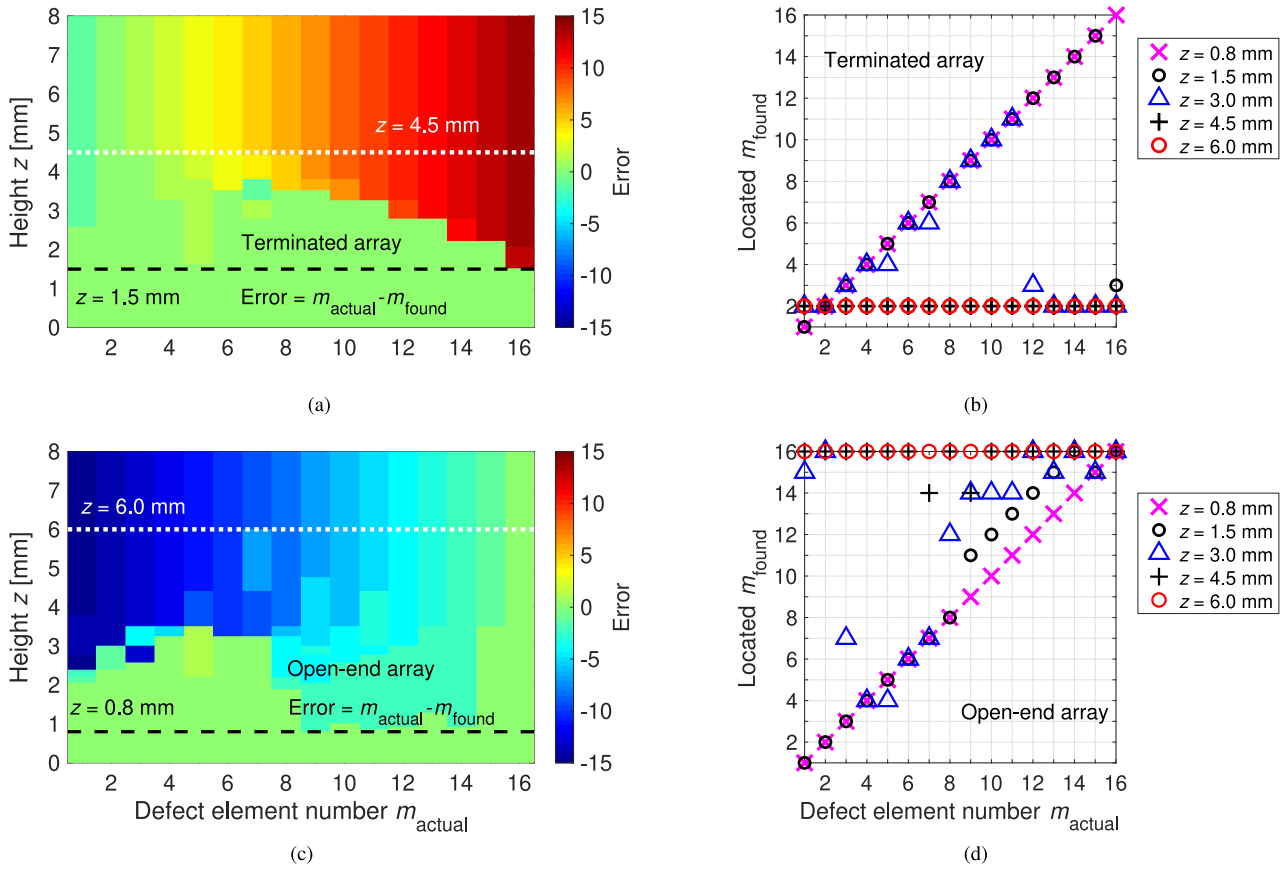

FIGURE 7. Results for accuracy in using the Odd-Even algorithm to localize metal objects on a 16-element array, using calculated reflectance spectrum. (a) and (b) are for an array with a matching termination, while (c) and (d) are for an open-end array with no termination. Both (a), (c) are coloured by the error ($m_{actual} - m_{found}$). As the object height is changed from 0 to 8 mm, L_{defect} varies from 15 to around 19.7 nH. The dashed black lines mark z = 1.5 mm for the terminated line, and z = 0.8 mm for the open array, which correspond to the maximum height up to which the localization error is zero. The dotted white lines mark z = 4.5 mm for the terminated case, and z = 6.0 mm for the open case, denoting the heights above which the found defect locations are always near either end of the array. For the terminated line, when z > 4.5 mm, m_{found} is always equal to 2, whereas m_{found} = 16 is always true if z > 6 mm for the open array. (b) and (d) illustrate the relationship between m_{found} and m_{actual}. The two quantities fall on a straight line for accurate localization, shown by the magenta crosses in both figures. As z increases, the interactions between the defect and the object becomes weaker, and more errors occur, as shown by the black circle (z = 1.5 mm), blue triangle (z = 3 mm), and black plus (z = 4.5 mm) markers.

resonator. Results from the Odd-Even algorithm are shown in the colourmap of Fig. 7 where the error $m_{\text{actual}} - m_{\text{found}}$ between the actual and derived locations is used to colour the map.

Fig. 7a, b are for an array terminated with a matching impedance. Fig. 7(a) is coloured by the error ($m_{\text{actual}} - m_{\text{found}}$) for varying object height z and defect location m_{actual}. We were able to localize the metal object on the terminated line

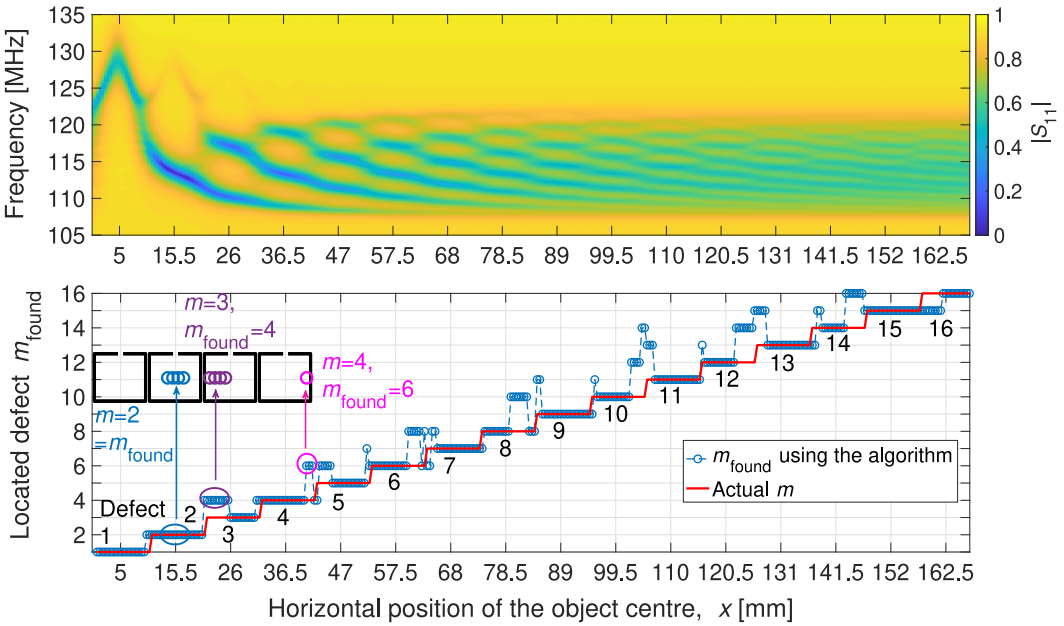

FIGURE 8. Measured S_{11} data for intermediate object locations is shown in the upper pane. The object is 0.4 mm above the sensor array, moved horizontally at 0.5 mm steps while S_{11} is measured. The horizontal position of the object centre is x. When $x = 0$, the centre of the object is above the track of the first excited element. The ticks for the x−axis, at $x = 5, 15.5, 26$ mm etc., show the object positions when the object is aligned with the element centres. The Odd-Even algorithm, though developed for localizing the metal object at registered locations, is tested for intermediate locations, using the measured data in the upper pane. The plot in the lower pane is for comparing the identified discrete locations using our algorithm (blue dashed line with circle markers) and the defined actual defect element number (red solid line). Here we define the defect element as the one that's under the object centre. As seen in the plot, errors in localization occur when the object is away from the element centres, and our algorithm, although devised for discrete localization, is robust when the object centre is within ±1 mm from the element centres.

accurately when the object is up to around 1.5 mm above the array, corresponding to $L_{\text{defect}} \approx 17.8$ nH. The Odd-Even algorithm completely fails when $z > 4.5$ mm, corresponding to $L_{\text{defect}} > 19.3$ nH. The reason is that the MIW approaches an infinite line and only one minimum can be found in $|\rho|$, therefore identifying all defect locations as position 2, as shown by the black plus signs and red circles in Fig. 7(b). Fig. 7(b) illustrates the relationships between m_{actual} and m_{found} for several z values. As z increases from 0.8 mm to 6 mm, the markers deviate from an oblique straight line, indicating the reduced accuracy.

Fig. 7c, d are for the same structure with no termination. In this case, we achieved accurate localization up to $z \approx 0.8$ mm ($L_{\text{defect}} \approx 16.9$ nH), shown by the magenta crosses falling on a straight line in Fig. 7(d). Above $z = 6$ mm, where $L_{\text{defect}} > 19.6$ nH, $m_{\text{found}} = 16$ for all actual defect locations, as shown in Fig. 7(d). The array approaches a uniform MIW with identical elements when the interactions with the metal object are so weak that the location of the object would have little impact on the calculated reflectance, as the structure approaches an undisturbed MIW.

Overall, the accurate localization up to $z = 0.8$ mm ($L_{\text{defect}} = 16.9$ nH) for a 16-element open array shows that our simple algorithm is reliable for strongly interacting objects. Correctly terminating the line with a matching termination, so that only the standing waves deriving from the object are present, improves this performance to $z = 1.5$ mm ($L_{\text{defect}} = 17.8$ nH).

The effect of waveguide bending on the propagation of MI waves has been investigated in [37]. Reflections are caused by abrupt bends in MI waveguides. Formulas for reflection and transmission coefficients were developed for various cases of bent structures in [37]. For our waveguide sensor, we expect that bending the array uniformly will not have strong impacts on its sensing performance. The nearest neighbour mutual coupling will change by the same amount for every pair of adjacent elements, resulting in a uniform array. The changes in non-nearest neighbour coupling might be inevitable but it could be kept low with careful designs of the structure.

If we had designed our sensing array as a flexible structure such as that described in [38], when the shape of the bent structure changes, the flexible hinges between adjacent elements ensure that the nearest neighbour coupling is unchanged, therefore the properties of the structure will stay nearly unaffected by the bending.

The tolerances of the transmission in an MIW have been analysed in [11]. The capacitance of each element is assumed to vary randomly so that the resonant frequencies of the elements are not identical. The frequency shifts in the resultant standing wave modes, and also the reduction in power transfer to a load due to a 5% change in the capacitances are not drastic. However, as pointed out in [11], other properties of the waveguide might be more sensitive to tolerances, and this needs to be addressed carefully in practical designs.

D. INTERMEDIATE LOCATIONS

We developed the Odd-Even algorithm based on the dispersion relationships, and it's expected to be valid for registered positions of the metal object. The measured S_{11} for intermediate object locations is shown in the upper pane of Fig. 8. The data for discrete locations (i.e., with the object above element centres) shown in Fig. 4(b) is a subset of the data presented in Fig. 8. In the measurement, we have the metal object 0.4 mm above the surface of the array, and the object is scanned at 0.5 mm steps horizontally across the array, with horizontal position $x = 0$ being the start position where the object centre is right above the side of the first element. At the marked positions $x = 5, 15.5, 26$ mm etc., the object centre is aligned with the centre of the defect element. As the object is moved between adjacent elements, the mutual coupling between adjacent cells and the resonances of the two cells are modified and require detailed characterization of the disturbed system to generalize the detection algorithm.

Although intermediate localization is out of the scope for this article, we tested our algorithm on the measured S_{11} data for intermediate locations of the metal object. When the object centre is above the area of one cell m, i.e., between its tracks, we define here the defect number as m, as illustrated in the inset to Fig. 8. Therefore object locations within ± 5 mm from the centre of a defect element should give the same outputs based on our algorithm. We compare the identified defect number using our algorithm (blue) with the actual defect number (red), shown in the lower figure of Fig. 8. Accurate localization is demonstrated when the object centre is aligned with element centres, or displaced by 0.5 mm closer to the source. And our algorithm is generally robust when the object centre is within 1 mm from the defect element centre, with a small error when element 8 is the defect. If we move the object away from the centre of each defect, errors start to appear, as expected. These results are much better than we expected. We tested our algorithm in violation of the approach, and yet robustness of the algorithm is shown. Based on the data shown in Fig. 8, approximately 73% of the intermediate object positions were identified, with the output being the correct defect element number. With proper analysis of the perturbed system and modifications to the algorithm, we believe that the accuracy of localization will certainly be improved.

IV. CONCLUSION

The sensitivity of meta-atoms to their environment makes the use of meta-atom arrays as sensors quite attractive. External nearby conducting objects affect the resonant characteristics of individual elements which can be readily modelled. Our resonant loop meta-atoms, tuned by mounted capacitors between the gap in the loop, are very sensitive to the proximity of highly conductive metal objects, modelled as the change in the self-inductance and the resistance of each element. A 1D array of magnetically coupled meta-atoms supports the propagation of magneto-inductive waves. Via MI waves we have been able to exploit this sensitivity to devise a spatial localization method for a metal object in one dimension. There is a single input port, also serving as the receiving port, to the MIW sensor. We are able to determine the location of a metal object using the standing wave patterns that it generates in the waveguide, which we observe with a single input point. An algorithm was developed and tested for its robustness in accurate localization of the metal object. We have shown through calculations that our Odd-Even algorithm works well for object height up to around 1.5 mm, if the structure is terminated properly to remove reflections from its end. This will be studied experimentally in the future. Localisation on a 1D array of a larger size will require more complex algorithms, and optimization may be required.

To detect a metal object larger than a single element in the sensor array, detailed characterizations are required for the resonances of the multiple perturbed elements under the object, and the change in the mutual coupling between adjacent cells as the object moves horizontally. While it may be possible to exploit superposition to deal with objects larger than one unit cell, this is likely to be quite limited by the strength of interaction between the object and the cells.

In addition, identifying the locations of multiple objects simultaneously positioned on the sensor is useful for multi-touch applications, which requires more detailed analysis. Multiple object detection is possible if the interactions between defect cells and the objects are weak. Overlaps in frequency between dips in the reflection spectrum from one defect and another will cause problems, and the defect closer to the source will be undetectable if we only use the corresponding frequencies as input to our localization algorithm. One possible solution is to make use of the full spectrum profile and take into account more comprehensive information in the algorithm. We will also extend the idea to devise a 2D MI sensing pad. The metal object used in this study is a bolt, the analysis of which can be extended to foreign objects of various types. A dielectric object, for example, can be detected and located by measuring S_{11} from a 1D structure consisting of open split ring resonators. The capacitance of unloaded resonators changes with the proximity of a dielectric object. A potential capacitive touch sensor can be made based on MI wave propagation in the structure.

The MI waves based position sensor has various practical applications. A new fluid level detector can be realized by fixing an array of coupled open split ring resonators on the inside of a container wall which is non-metallic, for instance. Embedded in a conveyor belt, a distributed metal detector can be made. In larger scales, where we aim to detect larger metal objects, such as charging pads for electric cars, position detection can be achieved by wrapping the 1D structure around the wheel and monitoring the changes in the standing wave patterns.

DATA AVAILABILITY

The research materials supporting this publication can be accessed by contacting the corresponding author J. Yan (e-mail: jiaruo.yan@eng.ox.ac.uk).

REFERENCES

[1] D. V. Redmayne, "Capacitive touch sensor," U.S. Patent 5 650 597 A, Jul. 1997. [Online]. Available: https://patents.google.com/patent/US5650597A/en

[2] S. Kim *et al.*, "A highly sensitive capacitive touch sensor integrated on a thin-film-encapsulated active-matrix oled for ultrathin displays," *IEEE Trans. Electron Devices*, vol. 58, no. 10, pp. 3609–3615, Oct. 2011.

[3] M. Schueler, C. Mandel, M. Puentes, and R. Jakoby, "Metamaterial inspired microwave sensors," *IEEE Microw. Mag.*, vol. 13, no. 2, pp. 57–68, Mar./Apr. 2012.

[4] M. Kang, J. Kim, B. Jang, Y. Chae, J.-H. Kim, and J.-H. Ahn, "Graphene-based three-dimensional capacitive touch sensor for wearable electronics," *ACS Nano*, vol. 11, no. 8, pp. 7950–7957, 2017.

[5] G. Barrett and R. Omote, "Projected-capacitive touch technology," *J. Soc. Inf. Display*, vol. 26, no. 3, pp. 16–21, 2010.

[6] T.-H. Hwang, W.-H. Cui, I.-S. Yang, and O.-K. Kwon, "A highly area-efficient controller for capacitive touch screen panel systems," *IEEE Trans. Consum. Electron.*, vol. 56, no. 2, pp. 1115–1122, May 2010.

[7] C. Stevens, J. Yan, and E. Shamonina, "A meta-material position sensor based on magneto-inductive waves," in *Proc. 13th Int. Congr. Artif. Mater. Novel Wave Phenomena (Metamaterials)*, Rome, Italy, Sep. 2019, p. 402.

[8] F. Hesmer *et al.*, "Coupling mechanisms for split ring resonators: Theory and experiment," *Physica Status Solidi (B)*, vol. 244, no. 4, pp. 1170–1175, 2007.

[9] L. Solymar and E. Shamonina, *Waves in Metamaterials*. Oxford, U.K.: Oxford Univ. Press, 2014.

[10] S. S. Bukhari, J. C. Vardaxoglou, and W. Whittow, "A metasurfaces review: Definitions and applications," *Appl. Sci.*, vol. 9, no. 13, p. 2727, 2019.

[11] E. Shamonina, V. A. Kalinin, K. H. Ringhofer, and L. Solymar, "Magnetoinductive waves in one, two, and three dimensions," *J. Appl. Phys.*, vol. 92, no. 10, pp. 6252–6261, 2002.

[12] J. Naqui, M. Durin-Sindreu, and F. Martin, "Novel sensors based on the symmetry properties of split ring resonators (SRRs)," *Sensors*, vol. 11, no. 8, pp. 7545–7553, 2011.

[13] J. Naqui, M. Durin-Sindreu, and F. Martin, "Alignment and position sensors based on split ring resonators," *Sensors*, vol. 12, no. 9, pp. 11790–11797, 2012.

[14] A. K. Horestani, J. Naqui, Z. Shaterian, D. Abbott, C. Fumeaux, and F. Martin, "Two-dimensional alignment and displacement sensor based on movable broadside-coupled split ring resonators," *Sensor Actuators A Phys.*, vol. 210, pp. 18–24, Apr. 2014.

[15] W. Withayachumnankul, K. Jaruwongrungsee, A. Tuantranont, C. Fumeaux, and D. Abbott, "Metamaterial-based microfluidic sensor for dielectric characterization," *Sens. Actuators A Phys.*, vol. 189, pp. 233–237, Jan. 2013.

[16] K. Shih, P. Pitchappa, M. Manjappa, C. P. Ho, R. Singh, and C. Lee, "Microfluidic metamaterial sensor: Selective trapping and remote sensing of microparticles," *J. Appl. Phys.*, vol. 121, no. 2, 2017, Art. no. 023102.

[17] P. Velez, L. Su, K. Grenier, J. Mata-Contreras, D. Dubuc, and F. Martin, "Microwave microfluidic sensor based on a microstrip splitter/combiner configuration and split ring resonators (SRRs) for dielectric characterization of liquids," *IEEE Sensors J.*, vol. 17, no. 20, pp. 6589–6598, Oct. 2017.

[18] M. Bakir *et al.*, "Microfluidic and fuel adulteration sensing by using chiral metamaterial sensor," *J. Electrochem. Soc.*, vol. 165, no. 11, pp. B475–B483, 2018.

[19] R. Melik, E. Unal, N. K. Perkgoz, C. Puttlitz, and H. V. Demir, "Metamaterial-based wireless strain sensors," *Appl. Phys. Lett.*, vol. 95, no. 1, 2009, Art. no. 011106.

[20] R. Melik, E. Unal, N. K. Perkgoz, C. Puttlitz, and H. V. Demir, "Metamaterial based telemetric strain sensing in different materials," *Opt. Exp.*, vol. 18, no. 5, pp. 5000–5007, 2010.

[21] M. U. Memon, A. Salim, H. Jeong, and S. Lim, "Metamaterial inspired radio frequency-based touchpad sensor system," *IEEE Trans. Instrum. Meas.*, vol. 69, no. 4, pp. 1344–1352, Apr. 2020.

[22] T. Floume, "Magneto-inductive conductivity sensor," *Metamaterials*, vol. 5, no. 4, pp. 206–217, 2011.

[23] V. S. Ramalingam, M. Kanagasabai, and E. F. Sundarsingh, "Detection of voids in fiber reinforced plastics using magnetoinductive coupled microstrip sensor," *IEEE Sensors J.*, vol. 15, no. 8, pp. 4182–4183, Aug. 2015.

[24] F. J. Herraiz-Martinez, F. Paredes, G. Z. Gonzalez, F. Martin, and J. Bonache, "Printed magnetoinductive-wave (MIW) delay lines for chipless RFID applications," *IEEE Trans. Antennas Propag.*, vol. 60, no. 11, pp. 5075–5082, Nov. 2012.

[25] R. R. A. Syms, E. Shamonina, and L. Solymar, "Magneto-inductive waveguide devices," *IEE Proc. Microw. Antennas Propag.*, vol. 153, no. 2, pp. 111–121, 2006.

[26] C. J. Stevens, C. W. Chan, K. Stamatis, and D. J. Edwards, "Magnetic metamaterials as 1-D data transfer channels: An application for magneto-inductive waves," *IEEE Trans. Microw. Theory Techn.*, vol. 58, no. 5, pp. 1248–1256, May 2010.

[27] C. Stevens, "Magnetoinductive waves and wireless power transfer," *IEEE Trans. Power Electron.*, vol. 30, no. 11, pp. 6182–6190, Nov. 2015.

[28] R. R. A. Syms, L. Solymar, and E. Shamonina, "Absorbing terminations for magneto-inductive waveguides," *IEE Proc. Microw. Antennas Propag.*, vol. 152, no. 2, pp. 77–81, 2005.

[29] R. R. A. Syms, L. Solymar, and I. R. Young, "Broadband coupling transducers for magneto-inductive cables," *J. Phys. D Appl. Phys.*, vol. 43, no. 28, 2010, Art. no. 285003.

[30] C. J. Stevens, Y. Li, and C. W. Chan, "Forward magneto-inductive wave propagation in planar magnetically coupled capacitor grids," *J. Electromagn. Waves Appl.*, vol. 29, no. 6, pp. 753–762, 2015.

[31] O. Sydoruk *et al.*, "Tailoring the near-field guiding properties of magnetic metamaterials with two resonant elements per unit cell," *Phys. Rev. B, Condens. Matter*, vol. 73, pp. 1–12, Jun. 2006.

[32] A. Radkovskaya *et al.*, "Dimer and polymer metamaterials with alternating electric and magnetic coupling," *Phys. Rev. B, Condens. Matter*, vol. 84, pp. 1–6, Sep. 2011.

[33] C. V. Dodd and W. E. Deeds, "Analytical solutions to eddy 'current probe' coil problems," *J. Appl. Phys.*, vol. 39, no. 6, pp. 2829–2838, 1968.

[34] A. Vallecchi, S. Chu, L. Solymar, C. J. Stevens, and E. Shamonina, "Coupling between coils in the presence of conducting medium," *IET Microw. Antennas Propag.*, vol. 13, no. 1, pp. 55–62, 2018.

[35] S. Chu, A. Vallecchi, C. J. Stevens, and E. Shamonina, "Fields and coupling between coils embedded in conductive environments," *EPJ Appl. Metamater.*, vol. 5, no. 2, p. 8, 2018.

[36] T. Hao, C. Stevens, and D. Edwards, "Optimisation of metamaterials by Q factor," *Electron. Lett.*, vol. 41, pp. 653–654, Jun. 2005.

[37] R. Syms and L. Solymar, "Bends in magneto-inductive waveguides," *Metamaterials*, vol. 4, no. 4, pp. 161–169, 2010.

[38] R. Syms, T. Floume, I. Young, L. Solymar, and M. Rea, "Flexible magnetoinductive ring mri detector: Design for invariant nearest-neighbour coupling," *Metamaterials*, vol. 4, no. 1, pp. 1–14, 2010.